

# Multiple charge transfer driven complex reaction dynamics: covalent bonding meets van der Waals interactions

Ruichao Dong<sup>1,2†</sup>, Xiaoqing Hu<sup>3†</sup>, Owen Dennis McGinnis<sup>4</sup>,  
Xincheng Wang<sup>1</sup>, Yikang Zhang<sup>1</sup>, Aha Chen<sup>1</sup>, Andreas Pier<sup>4</sup>,  
Alexander Tsertsvadze<sup>4</sup>, Huanyu Ma<sup>1</sup>, Jinze Feng<sup>1</sup>,  
Jessica Weiherer<sup>4</sup>, Laura Sommerlad<sup>4</sup>, Madeleine Schmidt<sup>4</sup>,  
Niklas Melzer<sup>4</sup>, Noah Kraft<sup>4</sup>, Sina Marie Jacob<sup>4</sup>, Zhenjie Shen<sup>1</sup>,  
Noelle Walsh<sup>5</sup>, Jianguo Wang<sup>3</sup>, Reinhard Dörner<sup>4</sup>,  
Kiyoshi Ueda<sup>1,7</sup>, Yong Wu<sup>3\*</sup>, Florian Trinter<sup>6\*</sup>, Till Jahnke<sup>4,8\*</sup>,  
Yuhai Jiang<sup>1,2,9\*</sup>

<sup>1</sup>Center for Transformative Science and School of Physical Science and Technology, ShanghaiTech University, No. 393 Middle Huaxia Road, Shanghai, 201210, China.

<sup>2</sup>Shanghai Advanced Research Institute, Chinese Academy of Sciences, No. 99 Haik Road, Shanghai, 201210, China.

<sup>3</sup>National Key Laboratory of Computational Physics, Institute of Applied Physics and Computational Mathematics, No. 2 Fenghao East Road, Beijing, 100088, China.

<sup>4</sup>Institut für Kernphysik, Goethe-Universität Frankfurt, Max-von-Laue-Str. 1, Frankfurt am Main, 60438, Germany.

<sup>5</sup>MAX IV Laboratory, Lund University, Box 118, Lund, 22100, Sweden.

<sup>6</sup>Molecular Physics, Fritz-Haber-Institut der Max-Planck-Gesellschaft, Faradayweg 4-6, Berlin, 14195, Germany.

<sup>7</sup>Department of Chemistry, Tohoku University, No. 41 Kawauchi, Sendai, 980-8578, Japan.

<sup>8</sup>Max-Planck-Institut für Kernphysik, Saupfercheckweg 1, Heidelberg, 69117, Germany.

<sup>9</sup>School of Physics, Henan Normal University, No. 46 Jianshe East Road, Xinxiang, 453007, Henan, China.

\*Corresponding author(s). E-mail(s): [wu\\_yong@iapcm.ac.cn](mailto:wu_yong@iapcm.ac.cn);  
[trinter@fhi-berlin.mpg.de](mailto:trinter@fhi-berlin.mpg.de); [jahnke@atom.uni-frankfurt.de](mailto:jahnke@atom.uni-frankfurt.de);  
[jiangyh3@shanghaitech.edu.cn](mailto:jiangyh3@shanghaitech.edu.cn);

†These authors contributed equally to this work.

### Abstract

The details of multiple charge transfer within or among molecules (including the accompanying molecular structure evolution and energy distribution) are typically not accessible on a single molecule level in experiments targeting complex condensed chemical or biological systems. In order to gather such detailed insight, small prototype systems that cover the essence of such processes need to be identified and investigated. Here, we employ a small system consisting of a combination of covalent and van der Waals bonds for our studies, namely  $\text{N}_2\text{Ar}$  dimers. We use synchrotron radiation to site-selectively enable the charge transfer processes and perform a coincidence measurement of the resulting electrons and ions. In combination with *ab initio* calculations, this approach enables a step-by-step tracking of the charge transfer and fragmentation dynamics. We find that ultrafast structural evolution of the dimer can trigger a second CT, thereby opening complex reaction pathways, in which electrons transfer back and forth between Ar and  $\text{N}_2$ , and nonadiabatic transitions occur twice through conical intersections. These results demonstrate that multiple CT-induced transitions, particularly in such a simple dimer system, provide benchmark insights into the mechanisms of nonadiabatic reactions in complex natural systems.

## 1 Introduction

Ultrafast charge transfer (CT), which redistributes electronic charge within or between molecular units, is one of the fundamental processes that underlie the emergence of function in natural and engineered systems [1–7]. Charge and energy transport span length scales from small dimers, simple and complex molecules in the gas or liquid phase to photoactive materials and proteins [8–13]. Tracing complex reactions induced by CTs is usually inaccessible via bulk ensemble measurements and the details of such vital processes remain poorly understood. Direct observation of (multiple) CTs at the single-molecule level is therefore essential, as it can offer unique insights into the process’ transient stages and unravel the most elementary quantum dynamics of both electrons and nuclei that participate in the complex process of charge transfer [14, 15].

In reality, the exchange of charge and energy occurs typically in complex systems, where covalent interactions and van der Waals bonding coexist normally. The van der Waals bond, the weakest noncovalent interaction, is ubiquitous in nature, governing the properties of nearly all organic solids and liquids [16–18]. It is responsible for phenomena such as the low boiling and melting points of substances, the layered structure of graphite, and the folding of DNA helices and proteins [19, 20], where multiple CTs across the interfaces of layers or molecules following optical excitation play

a fundamental role in the regulation of optoelectronic responses. Prototype systems for van der Waals bonds consist in many cases of rare gases. Simple rare-gas dimers, however, are not an ideal candidate to study the above mentioned reactions. Multiple CTs are even unexpected in these systems, since they tend to dissociate already at the instant of the first CT [21, 22]. A suitable prototype system for our studies is the  $\text{N}_2\text{Ar}$  dimer. It features a strong covalent bond between the two nitrogen atoms and a weak van der Waals bond between the argon atom and the  $\text{N}_2$  molecule. Its distinct properties make it a prototypical emulating model for experiment and quantum-chemical calculations to probe reaction mechanisms relevant to complex systems. First, the nearly matching ionization potentials [23, 24] of its two constituents make intermolecular reactions more effective under photoionization and photoexcitation scenarios by creating numerous crossings on the potential energy surfaces. Second, its structural flexibility, especially the stretching of its bonds [25] enables access to a manifold of nonadiabatic pathways through conical intersections and initiates the occurrence of multiple CT. Therefore, a system as simple as  $\text{N}_2\text{Ar}$  can effectively mimic the ensemble reactions occurring in complex condensed chemical and biological systems, with the Ar atom representing species of interest and the  $\text{N}_2$  molecule the environment.

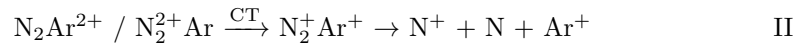
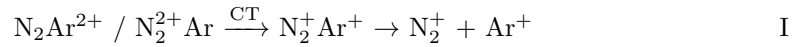
In more detail, in this single-molecule mixed-interaction system, it is possible to study multiple CT-induced bond cleavage and formation, novel reaction channels, and environmental reactions. Conversely, already a single CT (SCT) is a nontrivial process in this loosely bound entity: the transferred charge preferentially localizes at the Ar site rather than at the  $\text{N}_2$ , a topic studied for almost half a century [5, 25–29]. More recently, the formation of  $[\text{NAr}]^+$  was attributed to tunneling of a heavy  $\text{N}^+$  ion along the reaction  $[\text{N}_2\text{Ar}]^{2+} \rightarrow \text{N}^+ + [\text{NAr}]^+$  [30]. When  $[\text{N}_2\text{Ar}]^{2+}$  is created in collisions with highly charged ions, the double charge is expected to localize at the  $\text{N}_2$  site, raising questions about the interplay between CT and competing processes such as interatomic Coulombic decay. These surprising findings have sparked growing interest, but their underlying mechanisms remain unresolved.

X-ray-induced inner- or core-shell ionization offers an element-specific route to prepare this system in well-defined charge states. In this work, we investigate experimentally and theoretically the photoionization-induced nonadiabatic dynamics in  $\text{N}_2\text{Ar}$ , focusing on ultrafast multiple CT processes. Using datasets recorded at different photon energies (two in the X-ray and one in the XUV regime), we selectively initiate double ionization (DI) of either  $\text{N}_2$  or Ar via Auger decay or direct double ionization, thereby preparing well-defined initial states. By analyzing the momenta of dimer-fragments and electrons in the final state, we have unambiguously disentangled various CT pathways, enabling reconstruction of fragmentation pathways driven by SCT and double CT (DCT). Our findings demonstrate that even in such a simple dimer multiple CT-induced transitions can drive complex reaction channels, providing fundamental insight into charge redistribution as a core nonadiabatic mechanism underlying functional processes in complex natural systems.

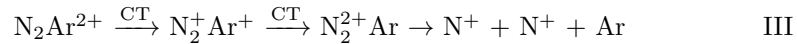
## 2 Expected charge transfer channels and involved potential energy surfaces

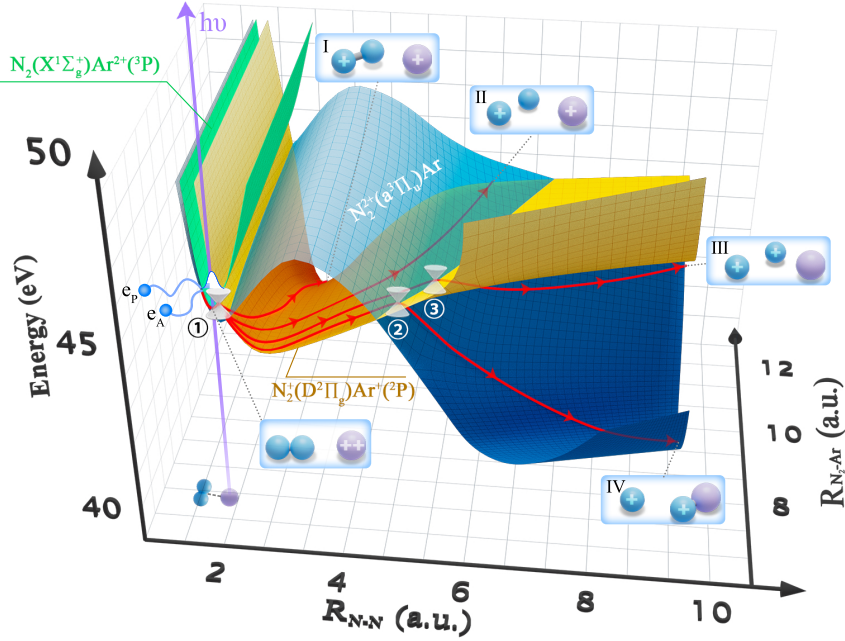
To gain intuitive insight into how the observed reaction channels – accompanied by ultrafast electron emission and CTs – are initiated and evolve from the doubly charged  $\text{N}_2\text{Ar}$  dimer, we calculated the corresponding potential energy surfaces (PESs) and traced the possible fragmentation pathways. Details on our calculations are provided in the Methods section. For  $[\text{N}_2\text{Ar}]^{2+}$ , charge localization can occur in three distinct configurations:  $\text{N}_2^{2+}\text{Ar}$ ,  $\text{N}_2\text{Ar}^{2+}$ , and  $\text{N}_2^+\text{Ar}^+$ . The high density of electronic states, together with the vibrational and rotational degrees of freedom of  $\text{N}_2$ , produces significant overlap among the PESs of these configurations across a wide range of  $\text{N}_2\text{Ar}$  bond lengths and angles. This extensive overlap facilitates exceptionally rapid non-adiabatic CT dynamics, a phenomenon rarely encountered in simpler systems such as  $\text{Ar}_2$  dimers. Selective ionization with X-ray photons of distinct energies enables preparation of specific initial states: removal of an N 1s or Ar 2p electron, followed by Auger decay, generates  $\text{N}_2^{2+}\text{Ar}$  states (e.g.,  $\text{X}^1\Sigma_g^+$ ,  $\text{a}^3\Pi_u$ ,  $\text{D}^1\Sigma_u^+$ ) or  $\text{N}_2\text{Ar}^{2+}$  states (e.g.,  $^3\text{P}$ ,  $^1\text{D}$ ,  $^1\text{S}$ ) [31, 32]. Subsequent intermolecular interactions drive structural evolution of the cluster ion, potentially leading to a nearly linear  $\text{N}_2\text{Ar}$  geometry.

Figure 1 presents the two-dimensional PESs for three electronic states of the linear  $[\text{N}_2\text{Ar}]^{2+}$  ion:  $(\text{N}_2^{2+}(\text{a}^3\Pi_u)\text{Ar})$ ,  $\text{N}_2(\text{X}^1\Sigma_g^+)\text{Ar}^{2+}(\text{}^3\text{P})$ , and  $\text{N}_2^+(\text{D}^2\Pi_g)\text{Ar}^+(\text{}^2\text{P})$ . When the system is initially prepared in either  $\text{N}_2^{2+}(\text{a}^3\Pi_u)\text{Ar}$  or  $\text{N}_2\text{Ar}^{2+}(\text{}^3\text{P})$ , the N-N vibrational wave packet lies within the crossing region with the  $\text{N}_2^+(\text{D}^2\Pi_g)\text{Ar}^+(\text{}^2\text{P})$  surface. This enables prompt SCT, producing the ion pair  $\text{N}_2^+ + \text{Ar}^+$ . Because the equilibrium bond length of  $\text{N}_2^+(\text{D}^2\Pi_g)$  is substantially larger than those of neutral  $\text{N}_2$  or  $\text{N}_2^{2+}(\text{a}^3\Pi_u)$ , the N-N bond elongates. At the same time, Coulomb repulsion in the pair  $\text{N}_2^+ + \text{Ar}^+$  drives a stretching of the  $\text{N}_2$ -Ar bond, thereby promoting dissociation along two distinct SCT pathways:

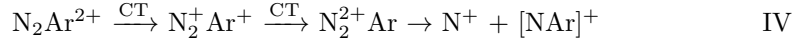


As the N-N bond continues to elongate, the PESs of  $\text{N}_2^+(\text{D}^2\Pi_g)\text{Ar}^+(\text{}^2\text{P})$  and  $\text{N}_2^{2+}(\text{a}^3\Pi_u)\text{Ar}$  intersect once more, enabling a second CT event. For clusters initially prepared in the  $\text{N}_2^{2+}(\text{a}^3\Pi_u)\text{Ar}$  state, dissociation proceeds via a two-step sequence: first,  $\text{N}_2^{2+}(\text{a}^3\Pi_u)$  captures an electron from Ar, forming  $\text{N}_2^+\text{Ar}^+$ ; subsequently, as the N-N bond stretches, an electron is transferred back to  $\text{Ar}^+$ , overcoming a substantial potential barrier. In contrast, for clusters initially in the  $\text{N}_2\text{Ar}^{2+}(\text{}^3\text{P})$  state, neutral  $\text{N}_2$  sequentially accepts two electrons from  $\text{Ar}^{2+}$ , ultimately driving dissociation. Remarkably, if the  $\text{N}_2$ -Ar distance remains sufficiently short after the second CT, the emerging  $\text{N}^+$  ion can bind to the neutral Ar atom, yielding a new  $[\text{NAr}]^+$  species via ion transfer. This secondary surface crossing therefore opens two additional dissociation pathways:





**Fig. 1 Schematic illustration of charge transfer processes from calculated potential energy surfaces (PESs).** Calculated PESs of the initial Auger final states,  $N_2(X^1\Sigma_g^+)Ar^{2+}(^3P)$  and  $N_2^+(a^3\Pi_u)Ar$ , produced following photoionization of the Ar 2p or N 1s shell, respectively. Ion pairs I ( $N_2^+$ ,  $Ar^+$ ) and II ( $N^+$ ,  $Ar^+$ , N) are generated via conical intersections between these initial states and the  $N_2^+(D^2\Pi_g)Ar^+(^2P)$  state. Subsequently, the ion pairs III ( $N^+$ ,  $N^+$ , Ar) and IV ( $N^+$ ,  $[NAr]^+$ ) emerge through two additional conical intersections involving the  $N_2^+(D^2\Pi_g)Ar^+(^2P)$  and  $N_2^+(a^3\Pi_u)Ar$  states. For clarity, the schematics highlight only the ionization pathways initiated at the Ar site.



As we show below, these fragmentation channels occur exclusively following photoionization of the Ar 2p shell. Notably, while Fig. 1 illustrates crossings among three representative electronic states, *ab initio* calculations of the adiabatic potential energy curves reveal dozens of intersecting states in this energy region, providing multiple pathways for both SCT and DCT processes.

### 3 Experimental Results and Discussion

In the following, we present the data recorded in two experimental campaigns, which were performed at the soft X-ray beamline P04 of PETRA III and the Flexible PhotoElectron Spectroscopy (FlexPES) beamline of MAX IV. We used a COLTRIMS reaction microscope [33, 34] for a coincident measurement of the momenta of electrons and ions generated after the absorption of the synchrotron light (see Materials and Methods for details). As indicated above, the doubly charged cluster ions,  $N_2Ar^{2+}$

or  $\text{N}_2^{2+}\text{Ar}$ , were produced via Auger decay following site-selective X-ray photoionization of the Ar 2p (260 eV) and N 1s (420 eV) shells, respectively. In addition, direct DI leading to  $\text{N}_2^{2+}\text{Ar}$  was investigated at a photon energy of 43.1 eV. At this photon energy, a direct DI at the Ar site is energetically forbidden [35, 36].

In Fig. 2 we present the time-of-flight correlation of two ions measured in coincidence with an electron. Panel (a) shows our results for a photon energy of  $h\nu = 260$  eV, while we used photons with an energy of 420 eV for the initial ionization of our gas target in Panel (b). In addition, we filtered both panels by requiring a photoelectron originating from the Ar and N<sub>2</sub> sites, respectively. A Coulomb explosion involving a breakup into exactly two ionic fragments – such as  $\text{N}_2^+ + \text{Ar}^+$ ,  $\text{N}^+ + [\text{NAr}]^+$  (and  $\text{N}^+ + \text{N}^+$  resulting from the ionization of uncondensed N<sub>2</sub> molecules) – the fragments are emitted back-to-back (i.e., with momenta of equal magnitude but opposite direction) due to momentum conservation, resulting in a sum momentum of the fragments of zero. This yields narrow diagonal features in the coincidence maps shown in Fig. 2 and used to identify the ion pairs occurring in the final state. In contrast, the  $\text{N}^+ + \text{Ar}^+ + \text{N}$  channel appears as a broader structure, since the undetected neutral N atom carries away a part of that sum momentum. In addition, the dissociation channel  $\text{N}^+ + \text{N}^+ + \text{Ar}$  is expected to overlap with the aforementioned  $\text{N}^+ + \text{N}^+$ -channel, but—as we show below—can be disentangled by our coincidence measurement.

We observe dimer fragmentation features belonging to all processes listed in Section 3.2 and labeled them accordingly in Figs. 2(a) and 2(b). In particular, we observe the breakup of the dimer after Ar 2p-ionization into  $\text{N}^+ + [\text{NAr}]^+$ , i.e., events belonging to channel IV that requires a double charge transfer and an ion transfer.

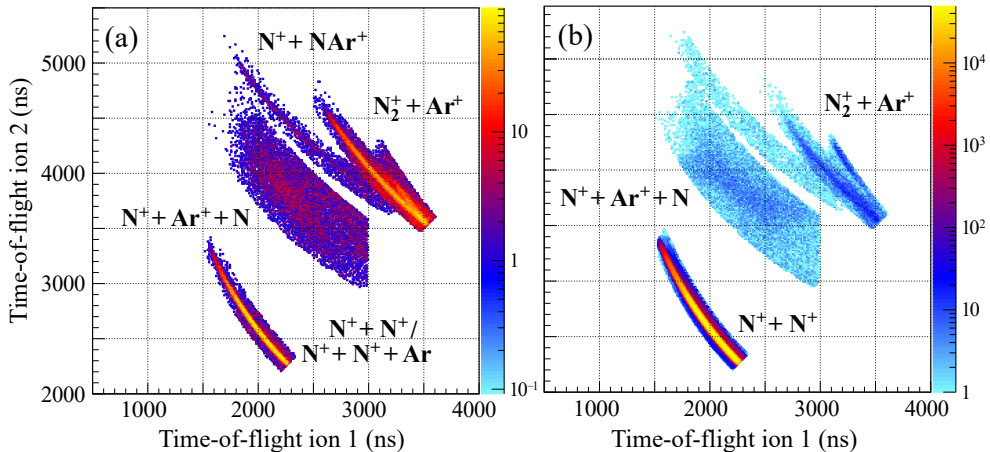


**Fig. 2 Measured three-body photoelectron-photoion-photoion coincidence spectrum.** Time-of-flight correlations of two ions detected in coincidence with a photoelectron from (a) Ar 2p photoionization at 260 eV and (b) N 1s photoionization at 420 eV. In panel (a), two additional fragmentation channels,  $\text{N}^+ + [\text{NAr}]^+$  and  $\text{N}^+ + \text{N}^+ + \text{Ar}$ , appear alongside the channels observed in both panels:  $\text{N}_2^+ + \text{Ar}^+$ ,  $\text{N}^+ + \text{Ar}^+ + \text{N}$ , and  $\text{N}^+ + \text{N}^+$ . The  $\text{N}^+ + \text{N}^+ + \text{Ar}$  and  $\text{N}^+ + \text{N}^+$  channels overlap in panel (a); their separation and analysis are discussed in Section 3.2.

### 3.1 Single Charge Transfer Pathways

To elucidate the mechanisms by which an electron is transferred across the dimer, we analyze the kinetic energy release (KER) spectra of the ionic fragments. Figure 3(a) shows the measured KER distribution for the  $\text{N}_2^+ + \text{Ar}^+$  channel associated with the SCT process, featuring a dominant peak at about 4.7 eV and a weaker peak at around 3.5 eV. In weakly bound systems, the KER resulting from a Coulomb explosion can be approximated by the Coulomb potential of two point-like charges that are located at a given internuclear distance  $R$ . Accordingly, within this approximation it is possible to extract internuclear distances from the measured KER. A KER of 3.5 eV corresponds to  $R = 4.11 \text{ \AA}$ , consistent with the equilibrium distance of  $R = 3.88 \text{ \AA}$  [37].

By contrast, the 4.7 eV peak corresponds to  $R = 3.06 \text{ \AA}$ , where  $\text{N}_2\text{Ar}^{2+}$  ions produced via Auger decay occupy an attractive region of the PES and SCT occurs at an internuclear distance significantly shorter (by  $0.82 \text{ \AA}$ ) than equilibrium [38]. This finding indicates that the CT proceeds on a timescale comparable to, or slower than, the vibrational motion of the cluster, consistent with the relatively large separation between constituents. Moreover, the  $\text{N}_2^+$  fragment in the  $\text{N}_2^+ + \text{Ar}^+$  channel can reside in a dissociative state, yielding the  $\text{N}^+ + \text{Ar}^+ + \text{N}$  channel. Figure 3(b) presents the corresponding KER distribution of the  $\text{N}^+$  and  $\text{Ar}^+$  fragments, which exhibits two peaks at 4.5 eV and 2.4 eV. The higher-energy peak reflects direct fragmentation of  $\text{N}_2^+$  following SCT, where essentially the entire Coulomb potential is shared between  $\text{N}^+$  and  $\text{Ar}^+$ , while the neutral N atom carries negligible kinetic energy. The resulting total KER closely matches the main peak in Fig. 3(a). In contrast, the lower-energy peak arises when  $\text{N}_2^+$  is at first repelled by the  $\text{Ar}^+$  as an intact entity and subsequently dissociates, with the neutral N atom removing about half the energy initially carried by  $\text{N}_2^+$ . This redistribution produces a smaller KER with a broader width.

To test whether the CT mechanism persists in more complex scenarios, we selectively ionized the  $\text{N}_2$  site in  $\text{N}_2\text{Ar}$  dimers using photons of 420 eV. Following N 1s photoionization, Auger decay produces doubly charged  $\text{N}_2^{2+}\text{Ar}$  ions. Figure 3(c) shows the measured KER distribution for the  $\text{N}_2^+ + \text{Ar}^+$  channel resulting from  $\text{N}_2$  site ionization. A KER of 3.5 eV corresponds to  $R = 4.11 \text{ \AA}$ , again consistent with the equilibrium separation of  $R = 3.88 \text{ \AA}$ , as illustrated in Fig. 1. Likewise,  $\text{N}_2^+$  ions formed from  $\text{N}_2^{2+}\text{Ar}$  via SCT can further dissociate into  $\text{N}^+ + \text{N}$  fragments, corresponding to pathway II in Fig. 1. As shown in Fig. 3(d), the KER distribution of  $\text{N}^+$  and  $\text{Ar}^+$  exhibits lower values and broader widths compared with the  $\text{N}_2^+ + \text{Ar}^+$  channel. This broadening arises because  $\text{N}_2^{2+}$  may begin to dissociate and release energy prior to the SCT event.

### 3.2 Double Charge Transfer Pathways

For the  $\text{N}^+ + \text{N}^+$  channel, one might initially assume that it arises from dissociation of  $\text{N}_2^{2+}$  produced by direct DI with a single 260 eV photon. However, the  $\text{N}^+ + \text{N}^+$  channel accompanied by a neutral Ar atom can instead be generated via DCT, as confirmed by our calculated PESs in Fig. 1. This assignment is further supported by our coincidence measurements with photoelectrons from Ar 2p inner-shell ionization, shown in Fig. 4(a). The solid blue line represents the total electron spectrum from all

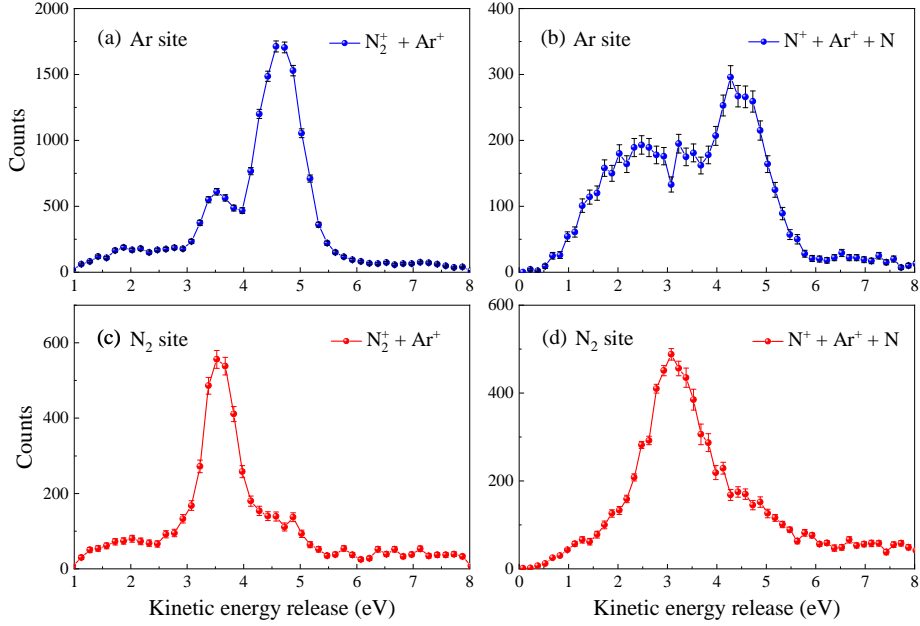


**Fig. 3 Kinetic energy release distributions of the fragment ions.** Measured KER spectra of two charged ions measured in coincidence with a photoelectron after breakup of the  $\text{N}_2\text{Ar}$  dimers into (a)  $\text{N}_2^+ + \text{Ar}^+$  and (b)  $\text{N}^+ + \text{Ar}^+ + \text{N}$  following Ar 2p photoionization at 260 eV, and into (c)  $\text{N}_2^+ + \text{Ar}^+$  and (d)  $\text{N}^+ + \text{Ar}^+ + \text{N}$  following N 1s photoionization at 420 eV. Error bars indicate statistical uncertainties.

events contributing to the  $\text{N}^+ + \text{N}^+$  channel, while the solid red line shows a partial electron spectrum obtained by applying momentum-conservation conditions to exclude events with  $|\sum p_z^i| \leq 5$  a.u. and  $|\sum p_z^i| \geq 20$  a.u., where  $p_z^i$  denotes the momentum of the  $i$ -th ion along the time-of-flight axis. The two distinct peaks observed in the red spectrum—absent in the blue—correspond to photoionization of the Ar  $2p_{3/2}$  and  $2p_{1/2}$  subshells [39]. This provides direct evidence that the  $\text{N}^+ + \text{N}^+$  channel originates from DCT processes in  $\text{N}_2\text{Ar}^{2+}$  ions, rather than from  $\text{N}_2^+\text{Ar}$ .

To further substantiate the presence of DCT processes, we compared the KER distribution of the  $\text{N}^+ + \text{N}^+ + \text{Ar}$  channel with that of the  $\text{N}^+ + \text{N}^+$  channel, as shown in Fig. 4(b). The solid blue and red lines correspond to the KER spectra of all  $\text{N}^+ + \text{N}^+$  ion pairs and of the partial ion pairs selected using the same momentum-conservation conditions as in Fig. 4(a), respectively. The two dominant peaks in the total-ion spectrum originate from the electronic states  $\text{D}^3\Pi_g$  and  $\text{D}^1\Sigma_u^+$  of  $\text{N}_2^{2+}$  at 7.7 eV and 10.3 eV, which are assigned to the dissociation channels producing  $\text{N}^+(^3\text{P}) + \text{N}^+(^3\text{P})$  and  $\text{N}^+(^3\text{P}) + \text{N}^+(^1\text{D})$ , respectively [31]. In addition to these two peaks, the partial-ion spectrum exhibits a distinct feature near 6 eV with a broad 3-7 eV envelope. This structure is attributed to the lower excited states of  $\text{N}_2^{2+}$ , such as  $\text{a}^3\Pi_u$  and  $\text{A}^1\Pi_u$ . Normally, dissociation of these states is difficult to detect because of their relatively

long lifetimes. However, through DCT processes they are populated at bond lengths already beyond the potential barrier, enabling prompt dissociation. The emergence of this new peak therefore provides unambiguous evidence that the partial fragments of  $N^+ + N^+$  originate from  $N_2Ar^{2+}$  via DCT, which agrees well with our simulated PESs.

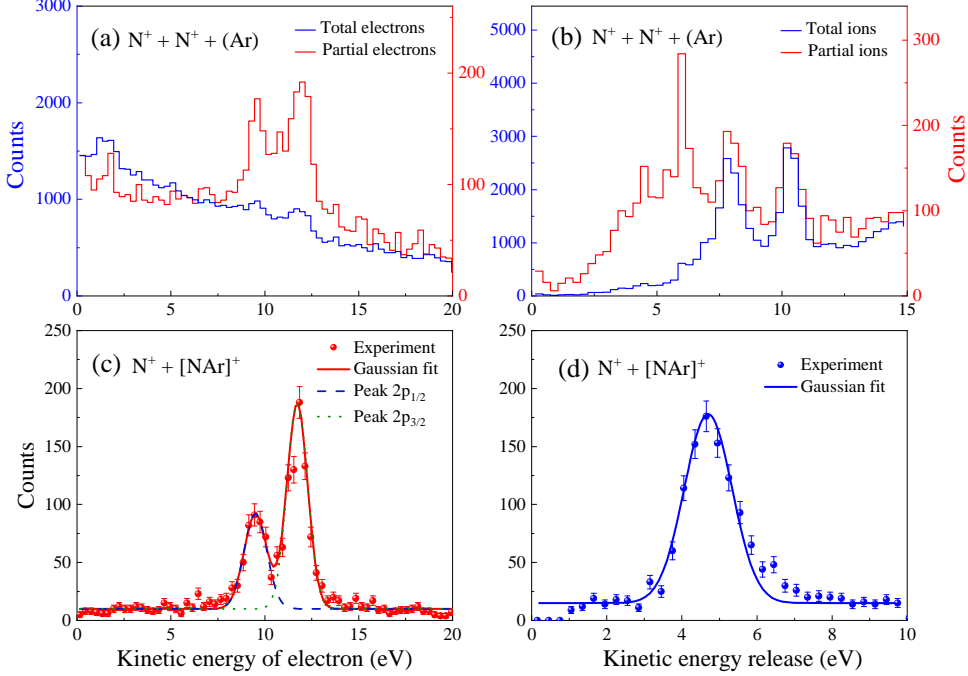


**Fig. 4 Kinetic energy distributions of the fragment ions and electrons.** (a) Measured electron kinetic energy and (b) KER spectra for  $N^+ + N^+$  pairs following Ar 2p or  $N_2$  valence DI at 260 eV. Shown are total events (blue line) and partial events (red line) selected by applying the momentum-conservation filter  $5 \text{ a.u.} < |\sum p_z^i| < 20 \text{ a.u.}$ , which effectively suppresses most background contributions from  $N_2$  monomer dissociation. The left and right  $y$  axes indicate event counts for total and partial electrons in (a) and ions in (b), respectively. (c) Measured electron kinetic energy and (d) KER spectra for  $N_2Ar$  dimer breakup into  $N^+ + [NAr]^+$  following Ar 2p photoionization at 260 eV. The two peaks in (c) correspond to photoelectrons from the Ar  $2p_{1/2}$  and Ar  $2p_{3/2}$  shells, respectively. Error bars represent statistical uncertainties.

Interestingly, an exotic heavy-ion transfer channel,  $N^+ + [NAr]^+$ , is observed in site-specific X-ray-produced  $N_2Ar^{2+}$  ions, as confirmed by the corresponding electron energy spectrum shown in Fig. 4(c). To unravel the reaction mechanism, we revisit the PESs of  $N_2Ar^{2+}$  shown in Fig. 1. Selective inner-shell ionization of the Ar atom efficiently populates the  $N_2(X^1\Sigma_g^+)Ar^{2+}(^3P)$  state. From there, the N–N vibrational wave packet evolves via a conical intersection into  $N_2^+(D^2\Pi_g)Ar^+(^2P)$ . As the wave packet proceeds further, the PESs of  $N_2^+(D^2\Pi_g)Ar^+(^2P)$  and  $N_2^+(a^3\Pi_u)Ar$  intersect at another conical intersection. Consequently,  $N_2^+(a^3\Pi_u)Ar$  is populated from the

initial Auger final state  $\text{N}_2(\text{X}^1\Sigma_g^+)\text{Ar}^{2+}(^3\text{P})$  through two sequential CT steps, i.e., a DCT process. The resulting  $\text{N}_2^{2+}\text{Ar}$  ions dissociate into  $\text{N}^+ + [\text{NAr}]^+$ , driven by Coulomb repulsion between the fragments. The measured KER spectrum [Fig. 4(d)] exhibits a peak at 4.7 eV. During  $[\text{NAr}]^+$  formation, all three atoms undergo substantial rearrangement; thus, the KER is not just given by Coulomb repulsion but also includes the vibrational energy of the  $[\text{NAr}]^+$  product. Because the DCT process does not involve intrinsic energy loss, the accessible KER range can be derived from the energy difference between the initial and final states. For reactions starting from  $\text{N}_2(\text{X}^1\Sigma_g^+)\text{Ar}^{2+}(^3\text{P})$ , this difference is approximately 6.45 eV when  $[\text{NAr}]^+$  is in its vibrational ground state, suggesting that the observed  $[\text{NAr}]^+$  carries 1.75 eV of vibrational excitation. The branching ratio of the  $\text{N}^+ + [\text{NAr}]^+$  channel reaches approximately 8% relative to the dominant  $\text{N}_2^+ + \text{Ar}^+$  channel, highlighting a significant probability of heavy-ion transfer even in a simple dimer system.

Other than for ionization at the Ar site, no DCT processes are observed following ionization at the  $\text{N}_2$  site. A likely explanation is that  $\text{N}_2^{2+}$  ions produced via Auger decay after N 1s ionization are predominantly short-lived states that undergo prompt dissociation driven by Coulomb repulsion [40]. For most of the final Auger states, the dissociation time scale of  $\text{N}_2^{2+}$  is shorter than the SCT timescale, thus suppressing the SCT process. This accounts for the markedly lower SCT signal in Figs. 3(c) and 3(d) compared with Ar site ionization in Figs. 3(a) and 3(b), even though the  $\text{N}_2$  site measurements were three times longer to compensate for differences in photoionization cross sections (N 1s at 420 eV vs. Ar 2p at 260 eV), yielding comparable total ionization counts. Likewise, the formation of  $[\text{NAr}]^+$  is not observed, since  $\text{N}_2^+(1s^{-1})$  rarely produces ground-state or low-lying excited  $\text{N}_2^{2+}$  via Auger decay. Instead, highly excited  $\text{N}_2^{2+}$  fragments into energetic  $\text{N}^+$  ions, which are unlikely to be captured by Ar. These findings indicate that rapid fragmentation of  $\text{N}_2$  can effectively suppress CT, although structural rearrangements within  $\text{N}_2$  could in principle facilitate multiple CT pathways.

One might argue that  $\text{N}_2^{2+}\text{Ar}$  could be produced directly via one-photon DI of the  $\text{N}_2$  site in  $\text{N}_2\text{Ar}$  dimers, subsequently leading to  $\text{N}^+ + [\text{NAr}]^+$ . To test this possibility, we performed an experiment with a photon energy of 43.1 eV, which lies above the DI threshold of  $\text{N}_2$  (42.8 eV), but below the DI threshold of Ar (43.37 eV). The results clearly show that the  $\text{N}^+ + [\text{NAr}]^+$  channel is absent, ruling out any contribution from one-photon DI of the  $\text{N}_2$  site at 260 eV as well. In contrast to the previously proposed heavy-ion tunneling scenario from  $\text{N}_2^{2+}\text{Ar}$  [30], our findings demonstrate that  $[\text{NAr}]^+$  formation proceeds via the DCT pathway described in expression IV, where electrons are transferred back and forth between the Ar and  $\text{N}_2$  sites through two successive nonadiabatic transitions at conical intersections.

## 4 Conclusion

In conclusion, we investigated ultrafast multiple CT processes mediated by nonadiabatic electron-nuclear dynamics in weakly bound systems using state-of-the-art coincidence spectroscopy in combination with *ab initio* calculations. Our investigations were performed using a prototype system that combines aspects of van der Waals and

covalent bonding: The  $\text{N}_2\text{Ar}$  dimer is complex enough to enable even double charge transfer processes and intriguing ultrafast molecular dynamics. Yet, its complexity is still suitable for a detailed study of these processes on a single-atom level. The intermolecular relaxation was initiated by site-selective ionization of the  $\text{N}_2$  molecule or the Ar atom within the dimer using photons in the X-ray and XUV regime. Both SCT and DCT processes were unambiguously identified experimentally and theoretically starting from well-defined initial states, namely  $\text{N}_2\text{Ar}^{2+}$  and  $\text{N}_2^{2+}\text{Ar}$ . The DCT pathways were experimentally established by observing the  $\text{N}^+ + \text{N}^+ + \text{Ar}$  and  $\text{N}^+ + [\text{NAr}]^+$  channels in coincident electron and ion energy spectra. For the latter case, a heavy  $\text{N}^+$  ion transfer channel was identified leading to the formation of  $[\text{NAr}]^+$ . This channel, observed experimentally in combination with calculations, is induced by DCT processes through two conical intersections in the  $\text{N}_2\text{Ar}^{2+}$  initial state but not in  $\text{N}_2^{2+}\text{Ar}$ . This mechanism fundamentally alters the character of CT in comparison to that of atom-atom dimers or clusters, where CT typically occurs only once. Our results thus demonstrate that sequential multiple CT processes, coupled to electron-nuclear dynamics, can drive ion transfer even in the simplest molecular aggregates. DCT was not observed in doubly charged  $\text{N}_2^{2+}\text{Ar}$  dimers, highlighting that rapid dissociation of molecular ions can suppress CT dynamics. Altogether, this study provides new insights into nonadiabatic intermolecular (multiple) CT dynamics, showing that even a simple single-molecule mixed-interaction system can undergo complex reaction pathways – an observation of broad relevance for understanding functional processes in complex biochemical systems.

## 5 Methods

**Experimental methods.** The experiments were performed using two synchrotron light sources at different photon energies: 260 eV and 420 eV were employed at the soft X-ray beamline P04 of the PETRA III synchrotron (DESY, Hamburg, Germany) in timing mode (40 bunches, 192 ns bunch separation) with circularly polarized light [41]; meanwhile, a photon energy of 43.1 eV was used at the Flexible PhotoElectron Spectroscopy (FlexPES) beamline of MAX IV (Lund, Sweden) in single-bunch mode (320 ns bunch separation) with linearly polarized light [42]. In both facilities, a supersonic gas jet was formed, collimated by two skimmers, and crossed with the photon beam inside a COLTRIMS reaction microscope [33, 34, 43], with  $\text{N}_2\text{Ar}$  dimers produced by expanding a 50/50 gas mixture through a 30  $\mu\text{m}$  nozzle at 11 bar (PETRA III) or a 50  $\mu\text{m}$  nozzle at 5 bar (MAX IV), both at 300 K. The employed COLTRIMS spectrometers consisted of an ion arm of 31 mm (PETRA III) or 34 mm (MAX IV) acceleration length and an electron arm of 70 mm acceleration and 153 mm drift length (Wiley-McLaren time-of-flight focusing geometry, PETRA III) or 419 mm acceleration length (MAX IV). All were equipped with microchannel plate detectors (active area of 120 mm diameter for the electron detector at PETRA III and of 80 mm diameter for all other detectors) with hexagonal delay-line position readout [44, 45]. Electrons and ions were guided to position-sensitive microchannel plate detectors with delay-line readout using optimized electric and magnetic fields, 20.8 V/cm and 5.6 G at PETRA III, and 12.4 V/cm and 7.7 G at MAX IV, allowing for the complete  $4\pi$

collection of electrons with kinetic energies up to 30 eV and 23 eV, respectively. Data were recorded in list mode files, measuring the positions and times of flight of all reaction products for each ionization event; this enabled the extraction of the weak dimer signals and the reconstruction of particle momenta in offline analysis, despite most events originating from monomer ionization, and charge transfer channels were ultimately identified by selecting events with two ions of equal and opposite momentum, whose sharp back-to-back emission line in the PIPICO spectrum provides a unique signature of the final Coulomb explosion step.

**Theoretical calculations.** The potential energy surfaces (PESs) of the linear  $[\text{N}_2\text{Ar}]^{2+}$  along the N–N bond were initially calculated using a two-body potential model [46]. This model incorporates only two-body correlation interactions, based on the known PESs of  $\text{N}_2$ ,  $\text{N}_2^{2+}$  and  $[\text{NAr}]^+$ , and neglects the three-body correlation. This approximation is justified for linear  $\text{N}_2\text{Ar}$  because one N atom is far from the Ar atom, rendering the three-body interaction negligible. To ensure higher precision, we subsequently performed *ab initio* calculations of the PESs of linear  $[\text{N}_2\text{Ar}]^{2+}$ ,  $\text{N}_2$ ,  $\text{N}_2^{2+}$ , and  $[\text{NAr}]^+$ . These calculations utilized the multi-reference double excitation configuration interaction (MRD-CI) method [47] with molecular orbitals optimized via the complete active space self-consistent field (CASSCF) method [48–50]. The active space comprised all valence orbitals, and approximately 1,000 reference configuration state functions were included in the CI calculations. The orbital wave functions were expanded in the aug-cc-pVTZ basis set. The resulting potential energy curves for linear  $[\text{N}_2\text{Ar}]^{2+}$  are provided in the Supplementary Information.

**Supplementary Information.** The Supplementary Information contains the resulting potential energy curves for the linear  $[\text{N}_2\text{Ar}]^{2+}$  configuration.

**Acknowledgements.** This work was supported by the National Key Research and Development Program of China (No. 2022YFA1604302), the National Natural Science Foundation of China (No. 12334011, No. 12204498, No. 12474259, No. 12374262, and No. 12450404), and the Natural Science Foundation of Henan (No. 252300421304). F.T. acknowledges funding by the Deutsche Forschungsgemeinschaft (DFG, German Research Foundation) – Project 509471550, Emmy Noether Programme.

We acknowledge DESY (Hamburg, Germany), a member of the Helmholtz Association HGF, for the provision of experimental facilities. Parts of this research were carried out at PETRA III. We would like to thank Jörn Seltmann and Moritz Hoesch for assistance during the experiments. Beamtime was allocated for proposal I-20240903. We acknowledge the MAX IV Laboratory for beamtime on the FlexPES beamline under proposal 20241221. Research conducted at MAX IV, a Swedish national user facility, is supported by Vetenskapsrådet (Swedish Research Council, VR) under contract 2018-07152, Vinnova (Swedish Governmental Agency for Innovation Systems) under contract 2018-04969 and Formas under contract 2019-02496. We also acknowledge support from the SXFEL and SHINE projects.

## Declarations

- Conflict of interest/Competing interests (check journal-specific guidelines for which heading to use)  
The authors declare no competing interests.
- Data availability  
The data that support the plots within this article are available from the corresponding authors upon reasonable request.
- Code availability  
The code that supports the plots within this article is available from the corresponding authors upon reasonable request.
- Author contributions  
R.Dö., K.U., Y.W., F.T., T.J., and Y.J. supervised the project. R.Do., O.D.M., X.W., Y.Z., A.P., A.T., H.M., J.F., J.W., L.S., M.S., N.M., N.K., S.M.J., Z.S., N.W., K.U., F.T., T.J., and Y.J. performed the experiments. X.H., A.C., J.W., and Y.W. performed the simulations. R.Do., K.U., F.T., T.J., and Y.J. analyzed the data. R.Do., X.H., F.T., T.J., and Y.J. wrote the manuscript after in-depth discussions with K.U. and R.Dö. and with input from all the authors.

## References

- [1] Marcus, R.A.: Electron transfer reactions in chemistry. Theory and experiment. *Rev. Mod. Phys.* **65**, 599 (1993) <https://doi.org/10.1103/RevModPhys.65.599>
- [2] Erk, B., Boll, R., Trippel, S., Anielski, D., Foucar, L., Rudek, B., Epp, S.W., Coffee, R., Carron, S., Schorb, S., Ferguson, K.R., Swiggers, M., Bozek, J.D., Simon, M., Marchenko, T., Küpper, J., Schlichting, I., Ullrich, J., Bostedt, C., Rolles, D., Rudenko, A.: Imaging charge transfer in iodomethane upon x-ray photoabsorption. *Science* **345**, 288–291 (2014) <https://doi.org/10.1126/science.1253607>
- [3] Schnorr, K., Senftleben, A., Kurka, M., Rudenko, A., Schmid, G., Pfeifer, T., Meyer, K., Kübel, M., Kling, M.F., Jiang, Y.H., Treusch, R., Düsterer, S., Siemer, B., Wöstmann, M., Zacharias, H., Mitzner, R., Zouros, T.J.M., Ullrich, J., Schröter, C.D., Moshhammer, R.: Electron Rearrangement Dynamics in Dissociating  $I_2^{n+}$  Molecules Accessed by Extreme Ultraviolet Pump-Probe Experiments. *Phys. Rev. Lett.* **113**, 073001 (2014) <https://doi.org/10.1103/PhysRevLett.113.073001>
- [4] Boll, R., Schäfer, J.M., Richard, B., Fehre, K., Kastirke, G., Jurek, Z., Schöffler, M.S., Abdullah, M.M., Anders, N., Baumann, T.M., Sebastian Eckart, B.E., Fanis, A.D., Dörner, R., Grundmann, S., Grychtol, P., Hartung, A., Hofmann, M., Ichen, M., Inhester, L., Janke, C., Jin, R., Kircher, M., Kubicek, K., Kunitzki, M., Li, X., Mazza, T., Meister, S., Melzer, N., Montano, J., Music, V., Nalin, G., Ovcharenko, Y., Passow, C., Pier, A., Rennhack, N., Rist, J., Rivas, D.E., Rolles, D., Schlichting, I., Schmidt, L.P.H., Schmidt, P., Siebert, J., Strenger,

- N., Trabert, D., Trinter, F., Vela-Perez, I., Wagner, R., Walter, P., Weller, M., Ziolkowski, P., Son, S.-K., Rudenko, A., Meyer, M., Santra, R., Jahnke, T.: X-ray multiphoton-induced coulomb explosion images complex single molecules. *Nat. Phys.* **18**, 423–428 (2022) <https://doi.org/10.1038/s41567-022-01507-0>
- [5] Zhang, G., Lu, D., Ding, Y., Guan, L., Han, S., Guo, H., Gao, H.: Imaging of the charge-transfer reaction of spin-orbit state-selected  $\text{Ar}^+(^2\text{P}_{3/2})$  with  $\text{N}_2$  reveals vibrational-state-specific mechanisms. *Nat. Chem.* **15**, 1255–1261 (2023) <https://doi.org/10.1038/s41557-023-01278-y>
- [6] Gopakumar, G., Unger, I., Slavíček, P., Hergenahm, U., Öhrwall, G., Malerz, S., Céolin, D., Trinter, F., Winter, B., Wilkinson, I., Caleman, C., Muchová, E., Björneholm, O.: Radiation damage by extensive local water ionization from two-step electron-transfer-mediated decay of solvated ions. *Nat. Chem.* **15**, 1408–1414 (2023) <https://doi.org/10.1038/s41557-023-01302-1>
- [7] Muchová, E., Gopakumar, G., Unger, I., Öhrwall, G., Céolin, D., Trinter, F., Wilkinson, I., Chatzigeorgiou, E., Slavíček, P., Hergenahm, U., Winter, B., Caleman, C., Björneholm, O.: Attosecond formation of charge-transfer-to-solvent states of aqueous ions probed using the core-hole-clock technique. *Nat. Commun.* **15**, 8903 (2024) <https://doi.org/10.1038/s41467-024-52740-5>
- [8] Wörner, H.J., Arrell, C.A., Banerji, N., Cannizzo, A., Chergui, M., Das, A.K., Hamm, P., Keller, U., Kraus, P.M., Liberatore, E., Lopez-Tarifa, P., Lucchini, M., Meuwly, M., Milne, C., Moser, J.-E., Rothlisberger, U., Smolentsev, G., Teuscher, J., van Bokhoven, J.A., Wenger, O.: Charge migration and charge transfer in molecular systems. *Struct. Dyn.* **4**, 061508 (2017) <https://doi.org/10.1063/1.4996505>
- [9] Nazmutdinov, R.R., Shermokhamedov, S.A., Zinkicheva, T.T., Ulstrup, J., Xiao, X.: Understanding molecular and electrochemical charge transfer: theory and computations. *Chem. Soc. Rev.* **52**, 6230–6253 (2023) <https://doi.org/10.1039/D2CS00006G>
- [10] Coropceanu, V., Chen, X.-K., Wang, T., Zheng, Z., Brédas, J.-L.: Charge-transfer electronic states in organic solar cells. *Nat. Rev. Mater.* **4**, 689–707 (2019) <https://doi.org/10.1038/s41578-019-0137-9>
- [11] Gray, H.B., Winkler, J.R.: Electron transfer in proteins. *Annu. Rev. Biochem.* **65**, 537–561 (1996) <https://doi.org/10.1146/annurev.bi.65.070196.002541>
- [12] Gillett, A.J., Privitera, A., Dilmurat, R., Karki, A., Qian, D., Pershin, A., Londi, G., Myers, W.K., Lee, J., Yuan, J., Ko, S.-J., Riede, M.K., Gao, F., Bazan, G.C., Rao, A., Nguyen, T.-Q., Beljonne, D., Friend, R.H.: The role of charge recombination to triplet excitons in organic solar cells. *Nature* **597**, 666–671 (2021) <https://doi.org/10.1038/s41586-021-03840-5>

- [13] Kaufman, D., Chen, C.-Y., Tsao, C.-Y., Zhao, Z., Lavon, A., Payne, G.F., Bentley, W.E., Ben-Yoav, H.: Redox-mediated Biomolecular information transfer in single electrogenic biological cells. *Biosens. Bioelectron.* **262**, 116546 (2024) <https://doi.org/10.1016/j.bios.2024.116546>
- [14] Pullanchery, S., Kulik, S., Rehl, B., Hassanali, A., Roke, S.: Charge transfer across C–H $\cdots$ O hydrogen bonds stabilizes oil droplets in water. *Science* **374**, 1366–1370 (2021) <https://doi.org/10.1126/science.abj3007>
- [15] Flór, M., Wilkins, D.M., de la Puente, M., Laage, D., Cassone, G., Hassanali, A., Roke, S.: Dissecting the hydrogen bond network of water: Charge transfer and nuclear quantum effects. *Science* **386**, 4369 (2024) <https://doi.org/10.1126/science.ads4369>
- [16] Delrio, F., Boer, M., Knapp, J., Reedy, E., Clews, P., Dunn, M.: The role of van der waals forces in adhesion of micromachined surfaces. *Nat. Mater.* **4**, 629–34 (2005) <https://doi.org/10.1038/nmat1431>
- [17] Santra, B., Klimeš, J., Alfè, D., Tkatchenko, A., Slater, B., Michaelides, A., Car, R., Scheffler, M.: Hydrogen bonds and van der waals forces in ice at ambient and high pressures. *Phys. Rev. Lett.* **107**, 185701 (2011) <https://doi.org/10.1103/PhysRevLett.107.185701>
- [18] Cao, J.-w., Li, F.-y., Xia, W.-s., Bian, W.-s.: van der waals interactions in bimolecular reactions. *Chin. J. Chem. Phys.* **32**, 157–166 (2019) <https://doi.org/10.1063/1674-0068/cjcp1901007>
- [19] DiStasio, R.A., Lilienfeld, O.A., Tkatchenko, A.: Collective many-body van der waals interactions in molecular systems. *Proc. Natl. Acad. Sci. USA* **109**, 14791–14795 (2012) <https://doi.org/10.1073/pnas.1208121109>
- [20] Singh, G., Chan, H., Baskin, A., Gelman, E., Repnin, N., Král, P., Klajn, R.: Self-assembly of magnetite nanocubes into helical superstructures. *Science* **345**, 1149–1153 (2014) <https://doi.org/10.1126/science.1254132>
- [21] Matsumoto, J., Leredde, A., Flechard, X., Hayakawa, K., Shiromaru, H., Rangama, J., Zhou, C.L., Guillous, S., Hennecart, D., Muranaka, T., Mery, A., Gervais, B., Cassimi, A.: Asymmetry in Multiple-Electron Capture Revealed by Radiative Charge Transfer in Ar Dimers. *Phys. Rev. Lett.* **105**, 263202 (2010) <https://doi.org/10.1103/PhysRevLett.105.263202>
- [22] Ren, X., Jabbour Al Maalouf, E., Dorn, A., Denifl, S.: Direct evidence of two interatomic relaxation mechanisms in argon dimers ionized by electron impact. *Nat. Commun.* **7**, 11093 (2016) <https://doi.org/10.1038/ncomms11093>
- [23] Wu, J., Kunitski, M., Schmidt, L.P.H., Jahnke, T., Dörner, R.: Structures of N<sub>2</sub>Ar, O<sub>2</sub>Ar, and O<sub>2</sub>Xe dimers studied by Coulomb explosion imaging. *J. Chem.*

- Phys. **137**, 104308 (2012) <https://doi.org/10.1063/1.4750980>
- [24] Wu, J., Gong, X., Kunitski, M., Amankona-Diawuo, F.K., Schmidt, L.P.H., Jahnke, T., Czasch, A., Seideman, T., Dörner, R.: Strong Field Multiple Ionization as a Route to Electron Dynamics in a van der Waals Cluster. *Phys. Rev. Lett.* **111**, 083003 (2013) <https://doi.org/10.1103/PhysRevLett.111.083003>
- [25] Linnartz, H., Verdes, D., Maier, J.P.: Rotationally Resolved Infrared Spectrum of the Charge Transfer Complex  $[\text{Ar-N}_2]^+$ . *Science* **297**, 1166–1167 (2002) <https://doi.org/10.1126/science.1074201>
- [26] Nikitin, E.E., Ovchinnikova, M.Y., Shalashilin, D.V.: Vibronic approach to dynamics of charge transfer in the  $[\text{ArN}_2]^+$  system. *Chem. Phys.* **111**, 313–326 (1987) [https://doi.org/10.1016/0301-0104\(87\)80143-X](https://doi.org/10.1016/0301-0104(87)80143-X)
- [27] Kim, H., Bowers, M.T.: Energetics, structure and photodissociation dynamics of the cluster  $\text{Ar-N}_2^+$ . *J. Chem. Phys.* **93**, 1158–1164 (1990) <https://doi.org/10.1063/1.459179>
- [28] Candori, R., Cavalli, S., Pirani, F., Volpi, A., Cappelletti, D., Tosi, P., Bassi, D.: Structure and charge transfer dynamics of the  $(\text{Ar-N}_2)^+$  molecular cluster. *J. Chem. Phys.* **115**, 8888–8898 (2001) <https://doi.org/10.1063/1.1413980>
- [29] Hua, Z., Zhao, Y., Hu, G., Feng, S., Zhang, Q., Chen, Y., Zhao, D.: Probing the Charge-Transfer Potential Energy Surfaces by the Photodissociation of  $[\text{ArN}_2]^+$ . *J. Phys. Chem. Lett.* **12**, 4012–4017 (2021) <https://doi.org/10.1021/acs.jpcclett.1c00798>
- [30] Zhu, X., Hu, X., Yan, S., Peng, Y., Feng, W., Guo, D., Gao, Y., Zhang, S., Cassimi, A., Xu, J., Zhao, D., Dong, D., Hai, B., Wu, Y., Wang, J., Ma, X.: Heavy  $\text{N}^+$  ion transfer in doubly charged  $\text{N}_2\text{Ar}$  van der Waals cluster. *Nat. Commun.* **11**, 2987 (2020) <https://doi.org/10.1038/s41467-020-16749-w>
- [31] Lundqvist, M., Edvardsson, D., Baltzer, P., Wannberg, B.: Doppler-free kinetic energy release spectrum of  $\text{N}_2^{2+}$ . *J. Phys. B: At. Mol. Opt. Phys.* **29**, 1489 (1996) <https://doi.org/10.1088/0953-4075/29/8/013>
- [32] Werme, L.O., Bergmark, T., Siegbahn, K.: The  $L_{2,3}\text{MM}$  Auger Spectrum of Argon. *Phys. Scr.* **8**, 149 (1973) <https://doi.org/10.1088/0031-8949/8/4/004>
- [33] Dörner, R., Mergel, V., Jagutzki, O., Spielberger, L., Ullrich, J., Moshhammer, R., Schmidt-Böcking, H.: Cold Target Recoil Ion Momentum Spectroscopy: a ‘momentum microscope’ to view atomic collision dynamics. *Phys. Rep.* **330**, 95–192 (2000) [https://doi.org/10.1016/S0370-1573\(99\)00109-X](https://doi.org/10.1016/S0370-1573(99)00109-X)
- [34] Jahnke, T., Weber, T., Osipov, T., Landers, A.L., Jagutzki, O., Schmidt, L.P.H., Cocke, C.L., Prior, M.H., Schmidt-Böcking, H., Dörner, R.: Multicoincidence

- studies of photo and Auger electrons from fixed-in-space molecules using the COLTRIMS technique. *J. Electron Spectrosc. Relat. Phenom.* **141**, 229–238 (2004) <https://doi.org/10.1016/j.elspec.2004.06.010>
- [35] Eland, J.H.D.: Complete double photoionisation spectra of small molecules from TOF-PEPECO measurements. *Chem. Phys.* **294**, 171–186 (2003) <https://doi.org/10.1016/j.chemphys.2003.08.001>
- [36] Morishita, Y., Liu, X.-J., Saito, N., Lischke, T., Kato, M., Prümper, G., Oura, M., Yamaoka, H., Tamenori, Y., Suzuki, I.H., Ueda, K.: Experimental Evidence of Interatomic Coulombic Decay from the Auger Final States in Argon Dimers. *Phys. Rev. Lett.* **96**, 243402 (2006) <https://doi.org/10.1103/PhysRevLett.96.243402>
- [37] Wu, C., Wu, C., Song, D., Su, H., Xie, X., Li, M., Deng, Y., Liu, Y., Gong, Q.: Communication: Determining the structure of the N<sub>2</sub>Ar van der Waals complex with laser-based channel-selected Coulomb explosion. *J. Chem. Phys.* **140**, 141101 (2014) <https://doi.org/10.1063/1.4871205>
- [38] Küstner-Wetekam, C., Hu, X.Q., Marder, L., Schmidt, P., Ozga, C., Zindel, C., Otto, H., Peng, Y.G., Wang, J.G., Richter, C., Sisourat, N., Hergenhan, U., Knie, A., Ehresmann, A., Wu, Y., Hans, A.: Nature and impact of charge transfer to ground-state dications in atomic and molecular environments. *Phys. Rev. A* **104**, 042802 (2021) <https://doi.org/10.1103/PhysRevA.104.042802>
- [39] Kato, M., Morishita, Y., Oura, M., Yamaoka, H., Tamenori, Y., Okada, K., Matsudo, T., Gejo, T., Suzuki, I.H., Saito, N.: Absolute photoionization cross sections with ultra-high energy resolution for Ar, Kr, Xe and N<sub>2</sub> in inner-shell ionization regions. *J. Electron Spectrosc. Relat. Phenom.* **160**, 39–48 (2007) <https://doi.org/10.1016/j.elspec.2007.06.003>
- [40] Püttner, R., Fukuzawa, H., Liu, X.-J., Semenov, S.K., Cherepkov, N.A., Tanaka, T., Hoshino, M., Tanaka, H., Ueda, K.: State-dependent gerade/ungerade intensity ratios in the Auger spectrum of N<sub>2</sub>. *J. Phys. B: At. Mol. Opt. Phys.* **41**, 141001 (2008) <https://doi.org/10.1088/0953-4075/41/14/141001>
- [41] Viefhaus, J., Scholz, F., Deinert, S., Glaser, L., Ilchen, M., Seltmann, J., Walter, P., Siewert, F.: The Variable Polarization XUV Beamline P04 at PETRA III: Optics, mechanics and their performance. *Nucl. Instrum. Methods Phys. Res., Sect. A* **710**, 151–154 (2013) <https://doi.org/10.1016/j.nima.2012.10.110>
- [42] Preobrajenski, A., Generalov, A., Öhrwall, G., Tchapyguine, M., Tarawneh, H., Appelfeller, S., Frampton, E., Walsh, N.: FlexPES: a versatile soft X-ray beamline at MAX IV Laboratory. *J. Synchrotron Radiat.* **30**, 831–840 (2023) <https://doi.org/10.1107/S1600577523003429>

- [43] Ullrich, J., Moshhammer, R., Dorn, A., Dörner, R., Schmidt, L.P.H., Schmidt-Böcking, H.: Recoil-ion and electron momentum spectroscopy: reaction-microscopes. *Rep. Prog. Phys.* **66**, 1463 (2003) <https://doi.org/10.1088/0034-4885/66/9/203>
- [44] Jagutzki, O., Mergel, V., Ullmann-Pfleger, K., Spielberger, L., Spillmann, U., Dörner, R., Schmidt-Böcking, H.: A broad-application microchannel-plate detector system for advanced particle or photon detection tasks: large area imaging, precise multi-hit timing information and high detection rate. *Nucl. Instrum. Methods Phys. Res., Sect. A* **477**, 244–249 (2002) [https://doi.org/10.1016/S0168-9002\(01\)01839-3](https://doi.org/10.1016/S0168-9002(01)01839-3)
- [45] Jagutzki, O., Lapington, J.S., Worth, L.B.C., Spillman, U., Mergel, V., Schmidt-Böcking, H.: Position sensitive anodes for MCP read-out using induced charge measurement. *Nucl. Instrum. Methods Phys. Res., Sect. A* **477**, 256–261 (2002) [https://doi.org/10.1016/S0168-9002\(01\)01843-5](https://doi.org/10.1016/S0168-9002(01)01843-5)
- [46] Qiu, B., Ruan, X.: Molecular dynamics simulations of lattice thermal conductivity of bismuth telluride using two-body interatomic potentials. *Phys. Rev. B* **80**, 165203 (2009) <https://doi.org/10.1103/PhysRevB.80.165203>
- [47] Krebs, S., Buenker, R.J.: A new table-direct configuration interaction method for the evaluation of Hamiltonian matrix elements in a basis of linear combinations of spin-adapted functions. *J. Chem. Phys.* **103**, 5613–5629 (1995) <https://doi.org/10.1063/1.470544>
- [48] Werner, H.-J., Knowles, P.J., Knizia, G., Manby, F.R., Schütz, M.: Molpro: a general-purpose quantum chemistry program package. *Wiley Interdiscip. Rev.: Comput. Mol. Sci.* **2**, 242–253 (2012) <https://doi.org/10.1002/wcms.82>
- [49] Werner, H.-J., Knowles, P.J., Celani, P., et al.: Molpro: A package of ab initio programs. (Cardiff University, Cardiff, U.K. 2012). (2025)
- [50] Werner, H.-J., Knowles, P.J., Manby, F.R., Black, J.A., Doll, K., Heßelmann, A., Kats, D., Köhn, A., Korona, T., Kreplin, D.A., Ma, Q., Miller, T.F., Mitrushchenkov, A., Peterson, K.A., Polyak, I., Rauhut, G., Sibaev, M.: The Molpro quantum chemistry package. *J. Chem. Phys.* **152**, 144107 (2020) <https://doi.org/10.1063/5.0005081>